Correlation between ridge subduction and a fluid reservoir in the Hyuganada accretionary prism: insights from a passive seismic array

[1]Takeshi Akuhara
[2]Yusuke Yamashita
[3]Shukei Ohyanagi
[3]Yasunori Sawaki
[1]Tomoaki Yamada
[1]Masanao Shinohara

[1]Earthquake Research Institute, The University of Tokyo, Tokyo, Japan
[2]Disaster Prevention Research Institute, Kyoto University, Kyoto, Japan
[3]Graduate School of Science, Kyoto University, Kyoto, Japan

Corresponding author:
Takeshi Akuhara (akuhara@eri.u-tokyo.ac.jp)

Key points

- The shear wave velocity structures of the shallow Hyuganada accretionary prism were derived using a passive seismic array.
- A fluid reservoir with a lateral extension of >100km exists ~3–4 km below the seafloor.
- Faults induced by the subducting Kyushu–Palau Ridge act as fluid pathways, supplying fluids to the reservoir.

Abstract

Subducted reliefs, such as seamounts and ridges, affect fluid processes in accretionary prisms of subduction zones. The Kyushu–Palau Ridge subducts along with the Philippine Sea Plate in Hyuganada, which is one of the regions that are best suited for studying the role of subducting topography. This study investigates the shear wave velocity structure using an array of ocean-bottom seismometers (OBSs) with a 2 km radius. Teleseismic Green's functions and a surface wave dispersion curve are inverted to one-dimensional shear wave velocity structures using transdimensional inversion. The results indicate the presence of a low-velocity zone 3–4 km below the seafloor. The reduced shear wave velocities are consistent with a compressional velocity structure obtained in a previous seismic refraction survey. We conclude that the low velocities are representative of high pore fluid pressure. In addition, the resolved lithological boundaries exhibit a sharp offset that consistently appears across the OBS array, suggesting the presence of a blind fault beneath it. The predicted fault, which is located at the flank of the Kyushu–Palau Ridge and oriented roughly parallel to the ridge axis, is likely caused by the ridge subduction. The fracture caused by the ridge subduction may act as a fluid conduit, forming a fluid reservoir beneath the well-compacted sediment layers. The compilation of previous refraction surveys implies that the reservoir has a lateral extension of >100 km. Its spatial distribution roughly correlates with the ridge location, highlighting the significant role the ridge plays in the formation of the reservoir.

Plain language summary

Topographic irregularities of the seafloor, such as seamounts, can affect the water distribution in the subsurface when they enter subduction zones, but the details are not fully understood. This study investigated the subsurface structure in Hyuganada in the southwestern Japan subduction zone based on natural seismic and noise data recorded by a dense array of seafloor seismographs. The results reveal a region with reduced

seismic wave velocity at a depth of ~3–4 km below the seafloor, which may be a reservoir. The detailed examination of this zone with reduced velocity zone and the comparison with the results of previous studies indicate that this reservoir has a horizontal extension of more than 100 km. We propose that a series of faults created by subducting seamounts serves as a conduit that transports water to the reservoir.

Keywords
Hyuganada
Kyushu–Palau Ridge
Fluid reservoir
Transdimensional inversion
Ocean-bottom seismometer

1. Introduction

Fluids, which may influence the frictional properties of faults by increasing pore pressure, are crucial for understanding the subduction–accretion system. They have been associated with the seismic cycle (Van Dinther et al., 2013), the genesis of slow earthquakes (Saffer & Wallace, 2015), and wedge development (Wang & Hu, 2006). In recent years, the vital role of the subducted relief, such as seamounts and ridges, in hydrology has been emphasized. Seamounts reportedly induce fractures within the overriding plate, which increases the permeability (Chesley et al., 2021; Sahling et al., 2008; Sun et al., 2020). However, direct observations of the fluid distribution and faults affected by the subducting topographies have been limited, and further investigations are required to understand the subduction system.

Hyuganada, located in the westernmost southwestern Japan subduction zone, is one of the regions facing ridge subduction (Figure 1). The incoming Philippine Sea Plate hosts the Kyushu–Palau Ridge (KPR) with a NNW–SSE strike. The subducted portion of this ridge has been identified by seismological studies employing either passive or active seismic sources (Park et al., 2009; Yamamoto et al., 2013). The subduction of the KPR beneath the Kyushu started at 5 Ma; the convergence direction was almost parallel to the ridge axis and perpendicular to the trench (Mahony et al., 2011). At 1–2 Ma, the subduction direction slightly rotated counterclockwise; consequently, the subduction accompanies the right-lateral motion (Itoh et al., 1998; Yamazaki & Okamura, 1989). Slow earthquakes, also termed episodic tremors and slips, intermittently occur near the KPR with an interval of 1–3 years (Baba et al., 2020; Tonegawa et al., 2020; Yamashita et al., 2015, 2021). As suggested for other regions

worldwide, these slow earthquake activities may reflect a fluid-rich environment near the plate interface (Saffer & Wallace, 2015). However, little is known about the fluid processes (e.g., fluid sources, pathways, reservoirs) in this region.

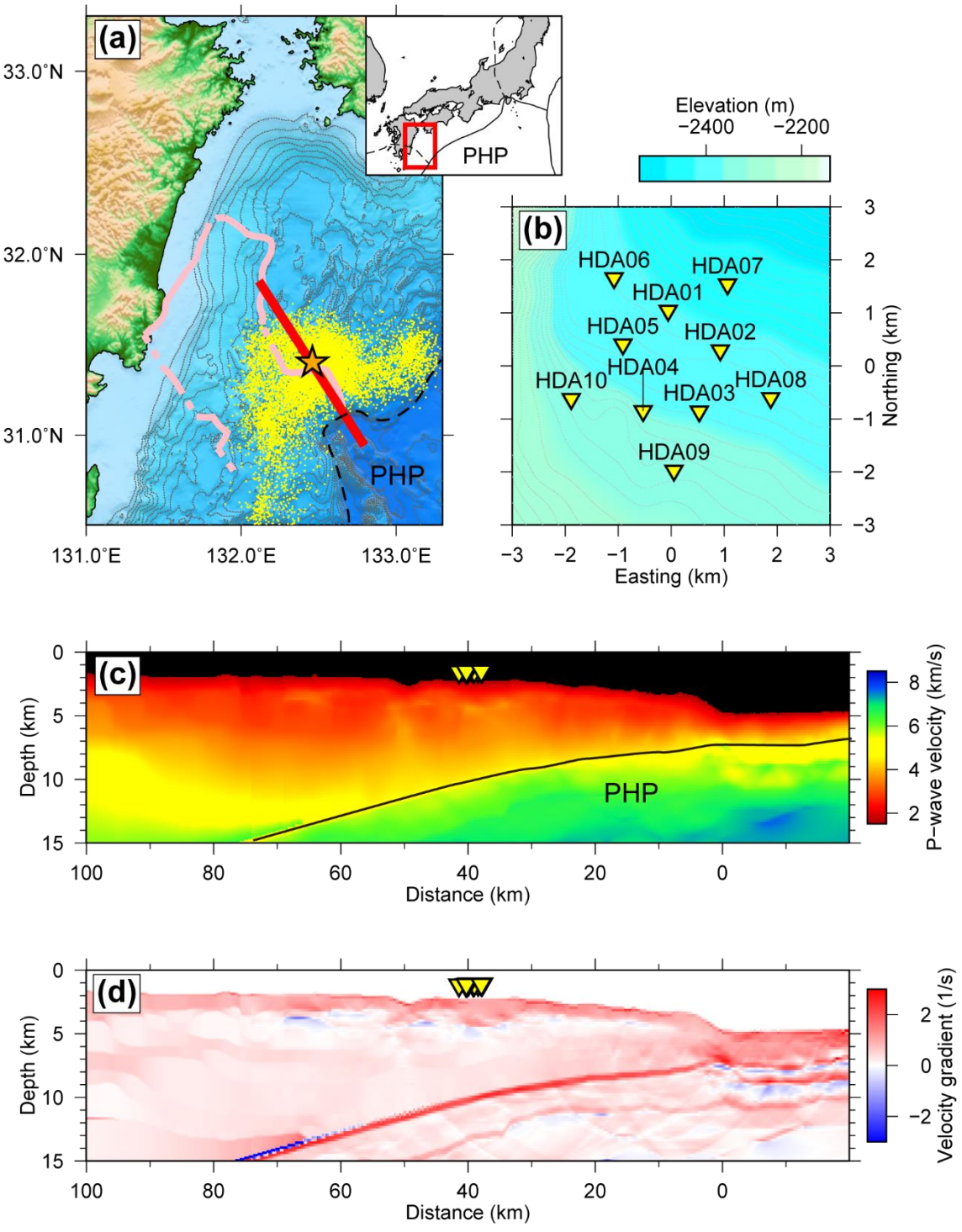

Figure 1. Tectonic setting of the study area and array configuration. (a) The orange star

denotes the location of an array of ocean-bottom seismometers. The red line represents the cross-section shown in (c) and (d). Yellow dots represent the epicenters of the tectonic tremors (Yamashita et al., 2015, 2021). The pink line denotes the subducting Kyushu-Palau Ridge (Yamamoto et al., 2013). (b) Array configuration. The gray contour indicates the water depth, with an interval of 10 m. (c) P-wave velocity model obtained from a refraction survey (Nakanishi et al., 2018). The yellow inverse triangles represent the locations of ocean-bottom seismometers. (d) The same as (c), but vertical velocity gradients are shown.

High-resolution structures of the accretionary prism in this region were obtained in previous active-source seismic surveys (Nakanishi et al., 2018; Nishizawa et al., 2009; Park et al., 2009). Figure 1c shows a P-wave velocity (Vp) model based on a refraction survey (Nakanishi et al., 2018). Overall, the accretionary prism shows a Vp of 2–4 km/s, which is typical. The subducting Philippine Sea Plate has a distinctive high velocity of >6 km/s beneath the prism. Interestingly, velocity inversion with depth is noticeable at ~2 km beneath the seafloor (Figure 1d). Nishizawa et al. (2009) have reported a similar low-velocity zone (LVZ) beneath another independent seismic profile in Hyuganada. These LVZs may indicate fluid-rich conditions, although a detailed interpretation has not been provided in previous studies. The challenges are the modest sensitivity of the refraction surveys to thin LVZs with a sharp velocity contrast and the interpretation of physical properties based on Vp alone.

This study investigates the shear wave velocity (Vs) structure by utilizing a dense passive seismic array of ocean-bottom seismometers (OBSs) deployed in the Hyuganada region. Traditionally, active-source seismic surveys play a central role in constraining Vs structures within shallow marine sediments. However, in contrast to Vp, investigating Vs via active seismic sources is challenging because of the inefficient excitation of shear waves beneath the seafloor. In recent years, various elements of passive seismic records have been increasingly used to overcome this problem, including ambient surface wave noise (Mosher et al., 2021; Tonegawa et al., 2017; Yamaya et al., 2021; Zhang et al., 2020), teleseismic body waves (Agius et al., 2018; Akuhara et al., 2020), and a combination of them (Doran & Laske, 2019). This study attempts to solve Vs structures through the transdimensional inversion of teleseismic body waves and a surface wave dispersion curve (DC). New information obtained about Vs provides further insights into subsurface rock properties, especially the pore fluid pressure. Based on the results, we discuss the hydrological features in Hyuganada, which can be linked to the subducting KPR.

2. Passive seismic array

This study uses a passive seismic array of 10 OBSs installed in the Hyuganada region. The OBSs continuously recorded seismic waveforms from March 30, 2018, to September 30, 2018 (Figure 1). Five OBSs (HDA01–05) were evenly installed within a radius of 1 km, whereas the other five OBSs (HDA06–10) were placed within 2 km, around the same center. Each OBS contains short-period three-component sensors (LE-3Dlite, Lennartz Electronic GmbH, Germany) and a gimbal to maintain the sensor horizontality. The seismometer positions were constrained by acoustic positioning from a research vessel. The sensor orientations were determined from the particle motion of teleseismic Rayleigh waves (Stachnik et al., 2012).

The array aimed to explore the potential of passive source methods for imaging shallow sediment structures. Another broadband OBS was deployed at the center of the array circle, but we failed to recover it. The array was placed on the refraction seismic survey line such that the tomography model could be used as a reference (Nakanishi et al., 2018; Figure 1). The seafloor topography is relatively gentle, with a slight slope to the northeast, resulting in a height difference of only ~120 m over the 4 km diameter (Figure 1b). Therefore, its effects on surface and body wave propagation are negligible.

3. Method

This section elaborates on procedures we adopted for the estimation of Vs structures beneath the OBSs. The DC measurements from ambient noise records are described in Section 3.1. In Section 3.2, we describe the procedure we used to retrieve the Green's function (GF) from teleseismic P-waves. Subsequently, the acquired DC and GFs were inverted to one-dimensional (1D) Vs structures using a transdimensional, stochastic inversion scheme, as discussed in Section 3.3.

3.1 Rayleigh wave dispersion curve

We retrievedRayleigh waves propagating across the array from half-year-long records of ambient seismic noise. For this purpose, we employ a series of signal processing steps: cutting records into 1 h long segments, detrending time series, downsampling data from 200 to 10 samples per second, deconvolution with instrumental responses, spectral whitening, and one-bit normalization in the time domain (Bensen et al., 2007). Cross-correlation functions (CCFs) are then calculated between each station pair and stacked over the entire observation period. We only use vertical-component

records for these processes because the short inter-station distances complicate the interpretation of horizontal component CCFs. Vertical component CCFs thus obtained are dominated by the fundamental Rayleigh mode at 0.1–0.5 Hz, with an apparent velocity of ~0.5 km/s (**Figure 2**).

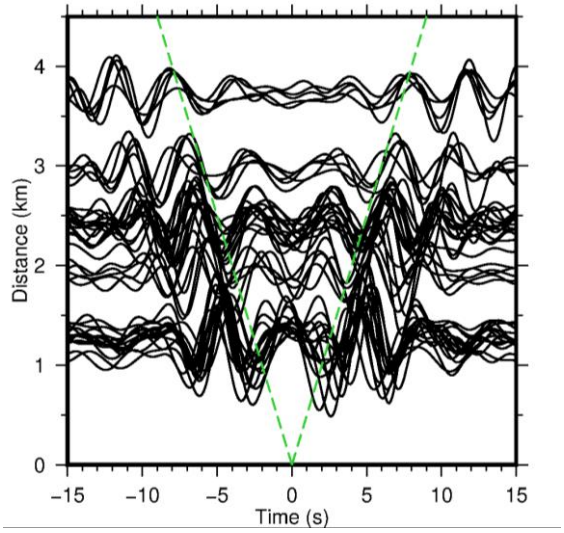

Figure 2. Ambient noise cross-correlation functions filtered from 0.2 to 0.4 Hz. The green line corresponds to a propagation speed of 0.5 km/s.

Based on the assumption of a laterally homogeneous structure beneath the array, the CCFs in Figure 2 can be considered to be virtual records from a linear array. These virtual records may be used for the frequency–wavenumber (FK) analysis (Gouédard et al., 2008). This treatment can significantly extend the high-frequency (or short-wavelength) limit of phase velocity measurements, without suffering from spatial aliasing effects. The shortest wavelength resolvable with FK techniques (λ_{min}) is typically twice the shortest station interval ($2d_{min}$). Based on the use of the virtual array, we can utilize short wavelengths down to ~0.002 km for the measurement of phase velocities, resulting in higher-frequency measurements. The acquisition of higher-frequency phase velocities is essential to constrain shallow structures within marine sediments.

The FK domain spectrum obtained from these virtual records shows the DC of the fundamental Rayleigh wave, which is traceable from 0.15 Hz (near the resolution limit) to 0.5 Hz (Figure 3). In the higher frequency range between 0.5–1.0 Hz, the spectrum exhibits a complex pattern, and it is hard to distinguish the actual signal from artificial sidelobes. A relatively continuous feature can be observed at a frequency of >1 Hz, corresponding to the higher-mode Rayleigh wave, but the mode identification is

nontrivial because of the ambiguity in the range of 0.5–1.0 Hz.

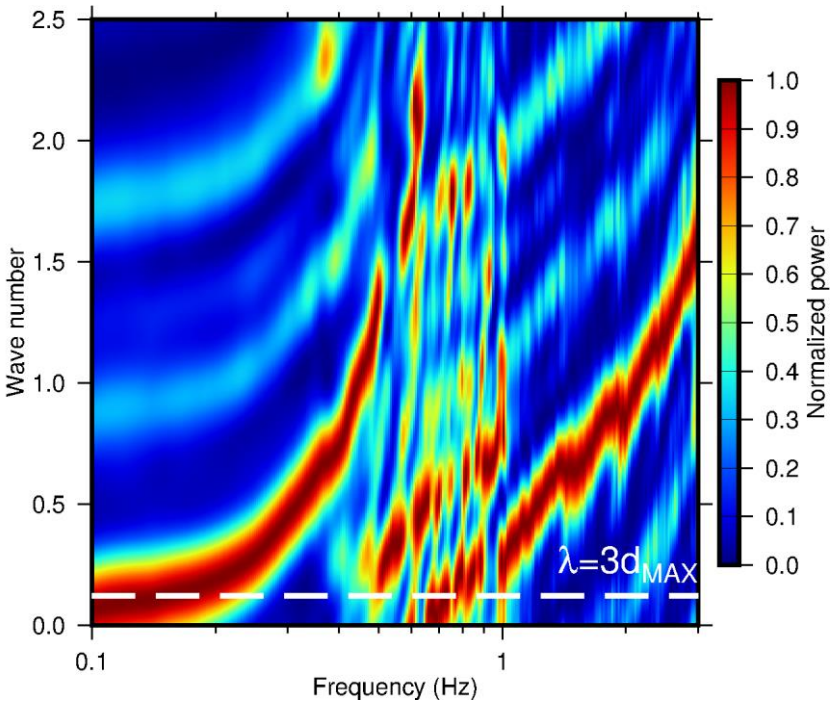

Figure 3. Frequency-wavenumber diagram calculated from ambient noise cross-correlations. The white dashed line indicates the resolution limit. Note that the power spectrum is normalized at each frequency.

3.2 Teleseismic Green's functions

We extract P waveforms of teleseismic events with M>5.5 and an epicentral distance of 30–90°. Each extracted record is decimated to 20 samples per second, and two horizontal components were rotated to radial and transverse directions. We only retain data with a signal-to-noise ratio (SNR) above 3.0 on the vertical component. In this study, the SNR is defined as the root-mean-square amplitude ratio of 30 s time windows before and after P arrival. The GFs of teleseismic P-waves are retrieved from these time windows with the blind deconvolution technique (Akuhara et al., 2019). In contrast to conventional receiver function methods that only solve radial-component GFs, both radial- and vertical-component GFs can be estimated with this method. The retrieval of vertical-component GFs is crucial for ocean-bottom settings because intense water multiples dominate the vertical-component records. We use 60 s time windows for the deconvolution and apply a Gaussian low-pass filter to the results. The Gaussian parameter (i.e., standard deviation) is set to 8, corresponding to a 10% gain at ~4 Hz.

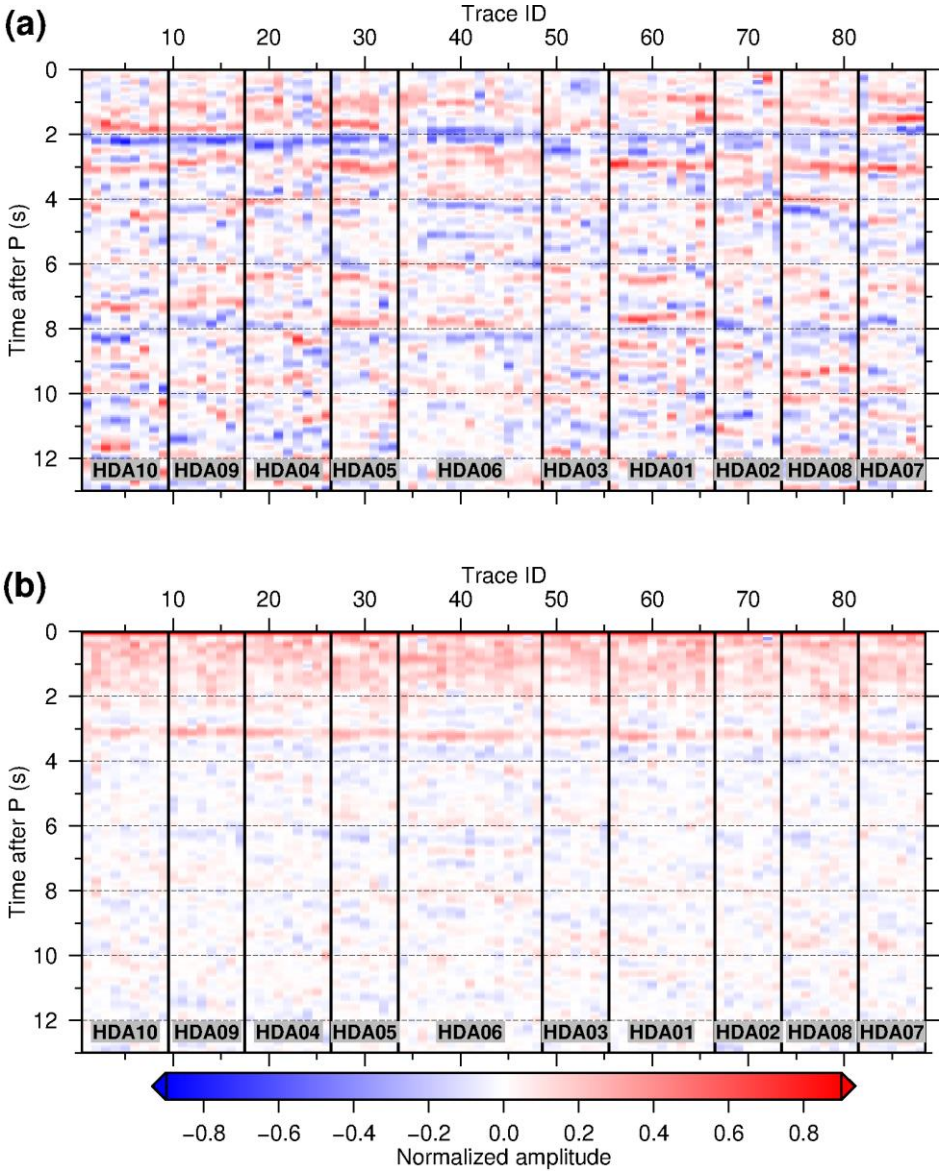

Figure 4. Green's functions estimated for teleseismic P-waves: (a) radial and (b) vertical components. The stations are sorted by their locations from WSW to ENE.

The radial-component GFs are mostly coherent across the array. A negative peak is predominant at ~2.0–2.5 s after the direct P arrival (Figure 4a). This coherency quantitatively justifies the 1D structure assumption we made for the FK analysis. At zero lag time, a peak corresponding to the direct P arrival is not evident, indicating the nearly vertical incidence of the P phase due to the low Vp of unconsolidated sediments. The vertical-component GFs show reverberations within the seawater column (Figure 4b). The first reverberation with a positive polarity is evident at 3.1 s, and the second

one can be observed at 6.2 s and has a reversed polarity. Although we did not use these vertical-component GFs for the inversion analysis, the good recovery of water reverberations to some degree validates the radial component estimations.

3.3 Transdimensional Bayesian inversion

We use a transdimensional Bayesian interface and the reversible-jump Markov chain Monte Carlo (RJMCMC) algorithm (Green, 1995) for the inversion of the dispersion and GF data to an isotropic 1D Vs model. The RJMCMC performs probabilistic sampling of model parameters, allowing the dimension of the model parameter space to be unknown. In our case, the algorithm automatically selects the number of layers in the 1D subsurface structure model. The transdimensional Bayesian inversion aims to estimate the posterior probability of the model parameter, $\boldsymbol{m}_k$, with the given data, $\boldsymbol{d}$, that is, $P(k, \boldsymbol{m}_k|\boldsymbol{d})$, where k is a parameter determining the model-space dimension. Based on the Bayes' theorem, the posterior probability is proportional to the product of the prior probability, $P(k, \boldsymbol{m}_k)$, and the likelihood, $P(\boldsymbol{d}|k, \boldsymbol{m}_k)$:

$$P(k, \boldsymbol{m}_k|\boldsymbol{d}) \propto P(k, \boldsymbol{m}_k)P(\boldsymbol{d}|k, \boldsymbol{m}_k).$$

3.3.1 Model parameters

We assume that the subsurface structure consists of k layers. Each layer has constant seismic P- and S-wave velocities and density; the structure's lateral heterogeneity, anisotropy, and dissipation are ignored. We defined a model vector $\boldsymbol{m}_k = (z_1, \cdots, z_{k-1}, \delta\beta_1, \cdots, \delta\beta_{k-1}, \sigma_{DC}, \sigma_{GF})^T$, where $\delta\beta_i$ is the S-wave velocity perturbation relative to a reference model and z_i is the bottom depth of the ith layer. The other two parameters, σ_{DC} and σ_{GF}, represent the standard deviations of data noise, which are also solved within the hierarchical Bayesian model (Bodin et al., 2012). Based on a given set of model parameters, first, a Vs value of each layer is extracted from the reference model. The perturbation $\delta\beta_i$ is then added to the extracted value. Similarly, Vp is obtained from the reference model, but without perturbation. The density is calculated from the Vp using an empirical relationship (Brocher, 2005). We fix the properties of the bottom half-space (i.e., kth layer) to stabilize the forward calculation of dispersion curves: Vs is set to 4.0 km/s and Vp and the density are scaled to Vs using the empirical law of Brocher (2005). For the seawater layer, we assume an acoustic velocity of 1.5 km/s and thickness of 2.388 km, which is the average station depth. The reference model was constructed from the two-dimensional (2D) P-wave velocity model of Nakanishi et al. (2008), as shown in Figure 1c, with the empirical

scaling law that converts Vp into Vs (Brocher, 2005).

3.3.2 Likelihood

We calculate the likelihood $P(\boldsymbol{d}|k,\boldsymbol{m}_k)$ based on the assumption of Gaussian noise distribution:

$$P(\boldsymbol{d}|k,\boldsymbol{m}_k) = P(\boldsymbol{d}_{DC}|k,\boldsymbol{m}_k)P(\boldsymbol{d}_{GF}|k,\boldsymbol{m}_k),$$

$$P(\boldsymbol{d}_{DC}|k,\boldsymbol{m}_k) = \frac{1}{\sqrt{(2\pi)^{N_{DC}}|\mathbf{C}_{DC}|}}\exp\left\{-\frac{1}{2}[\boldsymbol{g}_{DC}(k,\boldsymbol{m}_k)-\boldsymbol{d}_{DC}]^{\mathrm{T}}\mathbf{C}_{DC}^{-1}[\boldsymbol{g}_{DC}(k,\boldsymbol{m}_k)-\boldsymbol{d}_{DC}]\right\},$$

and

$$P(\boldsymbol{d}_{GF}|k,\boldsymbol{m}_k) = \frac{1}{\sqrt{(2\pi)^{N_{GF}}|\mathbf{C}_{GF}|}}\exp\left\{-\frac{1}{2}[\boldsymbol{g}_{GF}(k,\boldsymbol{m}_k)-\boldsymbol{d}_{GF}]^{\mathrm{T}}\mathbf{C}_{GF}^{-1}[\boldsymbol{g}_{GF}(k,\boldsymbol{m}_k)-\boldsymbol{d}_{GF}]\right\},$$

where $\mathbf{C}_{\mathrm{DC}}$ and $\mathbf{C}_{\mathrm{GF}}$ are the covariance matrixes of the DC and GF data noise, respectively, and $\boldsymbol{g}_{DC}$ and $\boldsymbol{g}_{GF}$ are the synthetic DC and GF, respectively. The data vector, $\boldsymbol{d}$, consists of DC and GF data vectors, denoted as $\boldsymbol{d}_{DC}$ and $\boldsymbol{d}_{GF}$, respectively, with a length of N_{DC} and N_{GF}, respectively. We assume the temporal correlation of noise for GFs, which originates from the Gaussian low-pass filter, and a constant noise level across the entire time series. The corresponding covariance matrix can be expressed by $\mathrm{C}_{\mathrm{GF}ij} = \sigma_{GF} r^{(j-i)^2}$, where r is pre-determined from the Gaussian filter width (Bodin et al., 2012) and σ_{GF} is a standard deviation of the data noise. We ignore off-diagonal components of the DC covariance matrix and assumed frequency-independent measurement error, which results in $\mathrm{C}_{\mathrm{DC}ij} = \sigma_{DC}\delta_{ij}$, where σ_{DC} is a standard deviation of DC data noise and δ_{ij} is the Kronecker delta. The standard deviations (i.e., σ_{DC} and σ_{GF}) are treated as hyper parameters and solved together with the model parameters with the hierarchical Bayesian model (Bodin et al., 2012).

3.3.3. Prior probabilities

We assume truncated uniform distributions for the prior probability of k, σ_{DC}, and σ_{GF}. We also assume the following limits: $[k_{min}, k_{max}) = [1, 41)$ for k, $[\sigma_{DCmin}, \sigma_{DCmax}] = [0.005, 0.090]$ for σ_{DC} (unit in km/s), and $[\sigma_{GFmin}, \sigma_{GFmax}] = [0.02, 0.07]$ for σ_{GF}. We confirmed that the resulting velocity structures are less affected by these choices. We set the minimum limit of the layer depths to z_{min} =2.388 (water depth) and the maximum to z_{max} =15 km and use the Dirichlet partition prior with unit concentration parameters (Dosso et al., 2014). This setting ensures that any combination of layer depths has an equal probability of occurring. We use the Gaussian

distribution with a zero mean for the Vs anomalies. The Gaussian width (i.e., standard deviation $\sigma_{\delta\beta}$) must reflect how reliable the reference model is. We set this parameter to 0.2 km/s. In summary, the joint prior can be expressed as follows:

$$P(k,\boldsymbol{m}_k) = \frac{1}{k_{max}-k_{min}} \cdot \frac{1}{\sigma_{DCmax}-\sigma_{DCmin}} \cdot \frac{1}{\sigma_{GFmax}-\sigma_{GFmin}} \cdot \frac{k!}{(z_{max}-z_{min})^k} \cdot \prod_{i=1}^{k-1} \frac{1}{\sigma_{\delta\beta}\sqrt{2\pi}} \exp\left(\frac{\delta\beta_i^2}{2\sigma_{\delta\beta}^2}\right).$$

3.3.4. Probabilistic sampling with parallel tempering

The RJMCMC algorithm aims to sample the posterior probability $P(k,\boldsymbol{m}_k|\boldsymbol{d})$ through iteration. At each iteration, a new model $(k',\boldsymbol{m}'_{k'})$is proposed by either (1) adding a layer, (2) removing a layer, (3) moving a layer interface, (4) perturbing the S-wave velocity of a layer, or (5) perturbing the standard deviation of the data noise. One of the above-mentioned five procedures is randomly selected at each iteration to generate a new model. The proposed model is accepted at a probability α_{MHG}, which is defined as the tempered Metropolis–Hastings–Green criterion (Green, 1995):

$$\alpha_{MHG} = \min\left\{1, \frac{P(k',\boldsymbol{m}'_{k'})}{P(k,\boldsymbol{m}_k)} \left[\frac{P(\boldsymbol{d}|k',\boldsymbol{m}'_{k'})}{P(\boldsymbol{d}|k,\boldsymbol{m}_k)}\right]^{\frac{1}{T}} \frac{Q(k,\boldsymbol{m}_k|k',\boldsymbol{m}'_{k'})}{Q(k',\boldsymbol{m}'_{k'}|k,\boldsymbol{m}_k)} |\boldsymbol{J}|\right\},$$

where $P(k,\boldsymbol{m}_k)$ is the prior probability; $Q(k',\boldsymbol{m}'_{k'}|k,\boldsymbol{m}_k)$ is the probability that a transition from $(k,\boldsymbol{m}_k)$ to $(k',\boldsymbol{m}'_{k'})$ is proposed; and $|\boldsymbol{J}|$ is the Jacobian compensating for a unit volume change in the model space. The exponent T (>1), which represents a temperature that loses the acceptance criterion, is a modification of the original Metropolis–Hastings–Green criterion. In the parallel tempering method (Geyer & Thompson, 1995; Sambridge, 2014), differently tempered Markov chains are run in parallel. At each iteration, a chain pair is probabilistically allowed to swap the temperatures. Based on this swap, the random walk can undergo a long jump in the model space and efficiently converge to the global maximum.

The inversion involves 500,000 iterations, including the first 100,000 iterations of the burn-in period. In total, 100 Markov chains are run in parallel, 20 of which have a unit temperature and are used to evaluate posterior probabilities. We only save the models every 1,000 iterations to avoid artificial correlation between samples.

4 Results

The ensemble of model parameters sampled by the transdimensional inversion

provides insights into the probable range of a 1D Vs structure beneath each station. Figure 5 shows the inversion results obtained at HDA06. The posterior marginal probability of Vs as a function of depth indicates a well-converged solution with a clearly defined peak at each depth. The velocity increases up to a depth of 4.8 km, with sharp, positive velocity contrasts at depths of 2.7 and 3.9 km. We conclude that these contrasts reflect different lithologies of sediments and refer to the layers as sedimentary units 1–3 (U1–3), from top to bottom.

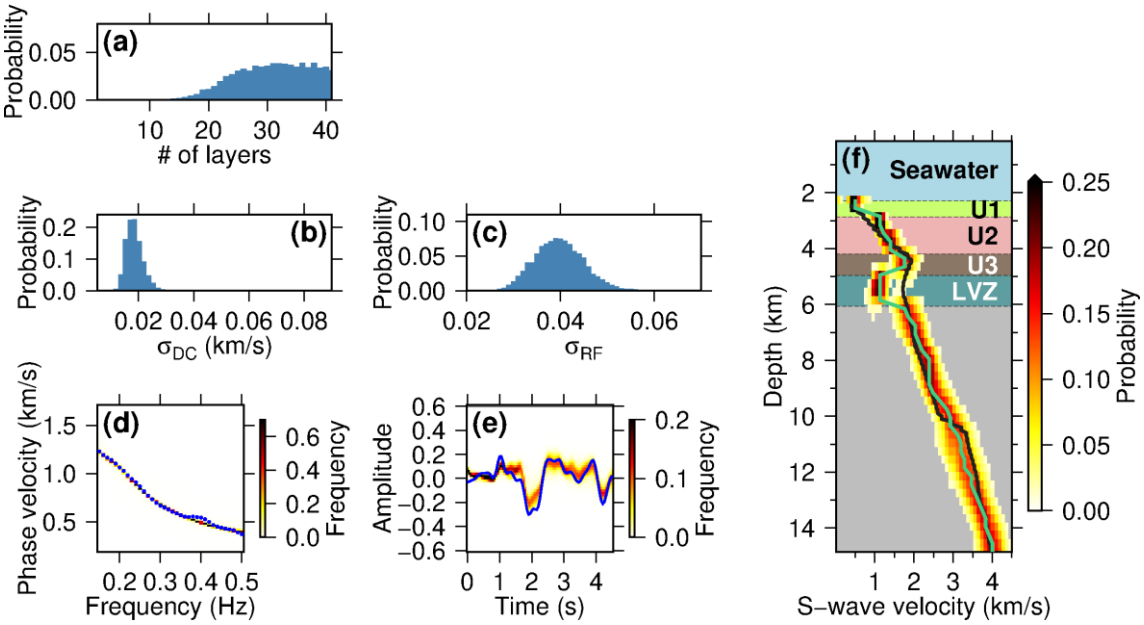

Figure 5. Joint inversion results for station HDA06. (a–c) Posterior probability of the (a) number of layers, (b) standard deviation of the noise in phase velocity data, and (c) standard deviation of the noise in Green's function data. (d–e) Input data (blue dots or curve) and model predictions (yellow–red heatmap) for the (d) dispersion curve and (e) Green's function. (f) Posterior marginal probability of the S-wave velocity as a function of depth. The yellow–red heatmap indicates the probability; low probabilities (<0.01) are transparently masked. The black line represents the reference velocity model. The green line indicates the mode estimation (i.e., the maximum probability at each depth). Background colors discriminate the different lithologies identified in this study.

Beneath this unit sequence, Vs abruptly drops to form a LVZ. The top of the LVZ is 0.1 km deeper than the depth at which the referenced Vp tomography model exhibits velocity inversion (see Figure 1d). Note that our prior Vs information already incorporates the velocity inversion that can be observed in the Vp model (black curve, Figure 5f). The inversion analysis requires the further reduction of Vs, suggesting a high

Vp/Vs ratio in the LVZ: based on the assumption of a Vp of 3.4 km/ s from the Vp tomography model, the Vp/Vs ratio corresponds to 2.8.

Inversion results from other stations show similar first-order features. Three layers (i.e., U1–3) are discernible immediately beneath the seafloor, and a LVZ can be detected beneath them (Figure 6). Exceptions are HDA01 without a LVZ and HDA03 exhibiting a high Vs (> 1 km/s) beneath the seafloor. The synthetic GFs for these two stations poorly fit the observations compared with those for the other stations (Figure 7c). Therefore, we excluded results for HDA01 and HDA03 from the discussion.

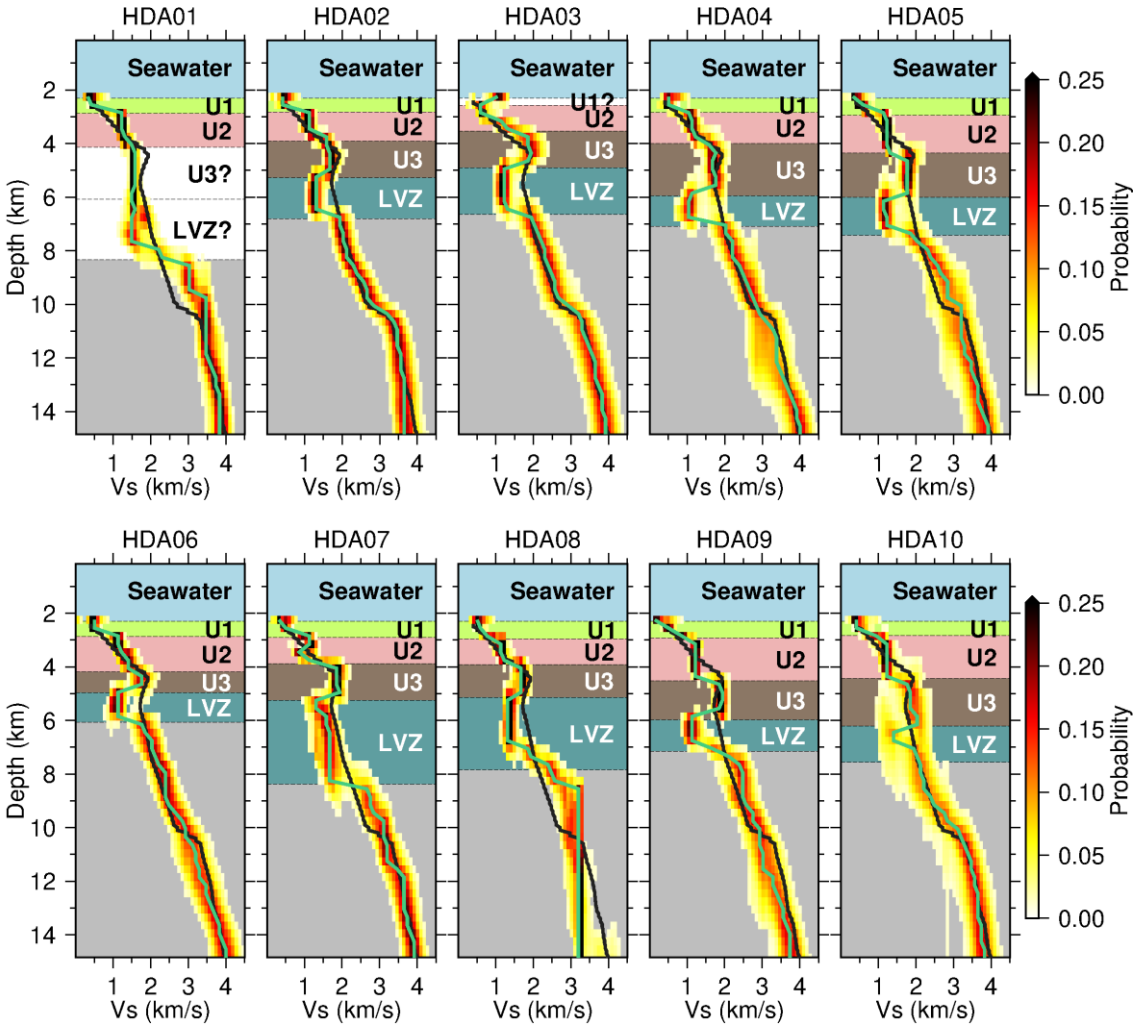

Figure 6. Joint inversion results for all stations. Each panel shows the posterior marginal probabilities of the S-wave velocity as a function of depth obtained for different stations. The notations are the same as those in Figure 5f.

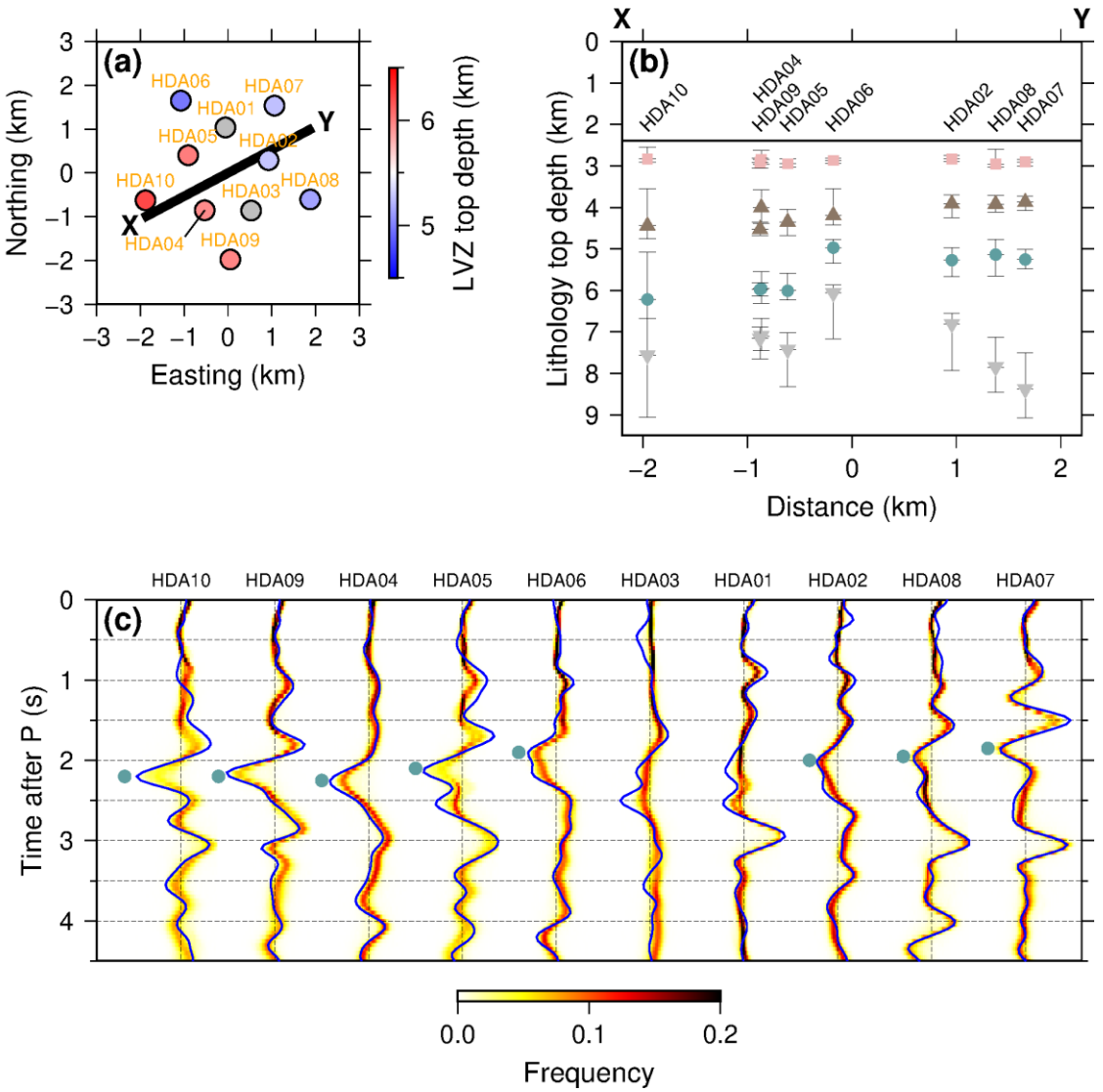

Figure 7. Lithology depths. (a) The depth of the top of the low-velocity zone (LVZ). The stations HDA01 and HDA03, whose velocity structures are inconsistent with the other stations, are masked in gray. (b) Lithology top depths along the profile X–Y shown in (a). The square, triangle, circle, and inverted triangle symbols denote the sedimentary units 2 (U2), 3 (U3), LVZ, and deeper lithology, respectively. The black line represents the average seafloor depth across the array. The stations HDA01 and HDA03 with suspicious results are not shown. (c) Teleseismic Green's function at each station. The blue wiggles represent the observed stacked GFs. The yellow–red heatmap represents the frequency distribution of the model predictions. The green circles indicate the negative peaks, which were interpreted as conversion phases from the top of the LVZ.

To quantify the depth of each lithological boundary, we searched for the depth of maximum velocity contrast within a given depth range. This search was performed for

all 1D S-wave velocity structures sampled in the inversion. The aggregation of all results provides statistics for the lithological boundary depths, such as median estimates and confidence intervals (Figures 5–7). We set the depth ranges for the search to 2.3–3.1 km for the boundary U1–U2, 3.1–5.5 km for U2–U3, 4.0–7.0 km for U3–LVZ, and 5.5–9.5 km for the bottom of the LVZ. Note that this error estimation tends to be biased toward magnifying uncertainties because the transdimensional inversion can produce ineffective (i.e., too thin) layers at random depths with a considerable velocity contrast. Hence, we chose to display the 68% confidence intervals in Figure 7b rather than the commonly used 95% intervals.

5. Discussion

5.1 Low-velocity zone indicative of high pore fluid pressure

The inversion results present a remarkable low-velocity feature with a velocity inversion. Typically, marine sediments undergo a monotonic increase in Vs with increasing depth because of compaction (Hamilton, 1979). The velocity inversion observed in this study is unexpected. A plausible cause for the observed velocity inversion is high pore fluid pressure. High pore pressure can significantly decrease Vs because shear waves do not propagate through pore spaces filled with fluids. Based on theory and experiments, it is known that high pore fluid pressure increases the Vp/Vs ratio of marine sediments (Dvorkin et al., 1999; Prasad, 2002), which agrees with our results.

Sustaining the overpressure condition within the LVZ will require a relatively impermeable structure above. In addition, structural elements effectively conveying fluid to the LVZ, such as faults and fractures, are essential if fluid sources reside outside the LVZ. Laboratory measurements on terrigenous sediments from deep-sea drilling have shown that the porosities gradually decrease with depth, from ~70% at the sea bottom to ~20% at a burial depth of 1.5 km (Kominz et al., 2011). Thus, we speculate that the bottom of Unit 3, with a burial depth of ~2.6–3.9 km, undergoes more severe porosity loss and can impede fluid to permeate shallower layers. This permeability barrier could trap abundant fluid below, leading to the formation of the LVZ. The presence of faults or fractures acting as fluid pathways seems likely in this region because of the stress load from the subducting KPR, as discussed in more detail in Section 5.2. Slow earthquakes occurring beneath the array may indicate a fluid-rich environment near the subducting plate interface (Saffer & Wallace, 2015), which possibly is a fluid source for the LVZ, as discussed later in Section 5.3.

5.2 Structural offset indicative of a blind fault

Qualitative estimates of uncertainties based on stochastic inversion confirmed the lateral variation in the depth of the top of the LVZ: the lithological boundary deepens on the southwestern side, whereas it becomes shallower on the northeastern side (Figure 7a). The GF waveforms support such a lateral variation, where a negative phase corresponding to Ps conversion from the top of the LVZ arrives at the northeastern stations (HDA06, 02, 08, and 07) ~0.5 s earlier than at the southwestern stations (HDA10, 09, 04, and 05), as shown in Figure 7c. Although less notable, a similar offset occurs in a subparallel manner at the top of U3 (Figure 7b). Because of its sharpness (~1 km vertical offset within a distance of 0.5 km), consistency over the different lithological boundaries, and linearity in the map view, we conclude that this offset indicates the presence of a blind fault (Figure 8b). The fault may act as a fluid conduit and contribute to the formation of the LVZ. The large offset (~1 km) might suggest that the fault has been repeatedly activated over millions of years after the ridge subduction.

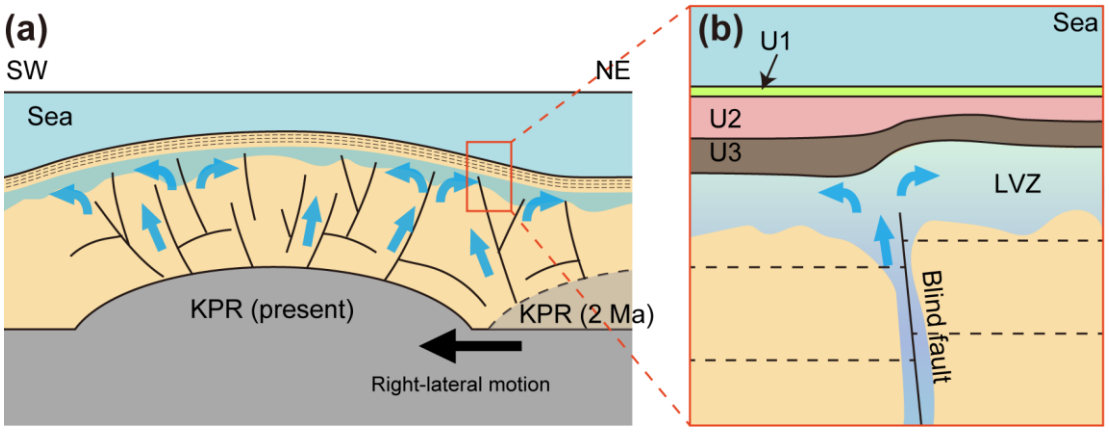

Figure 8. Schematic illustration of the hydrology based on the results of this study. The sky-blue arrows depict fluid flow. (a) Macroscopic view. Numerous faults induced by the subducted Kyushu–Palau Ridge act as fluid conduits to form a fluid reservoir with a wide extension in the Hyuganada region. (b) Enlarged view beneath the OBS array. The offset in the lithological boundaries suggests the presence of a blind fault.

Because our data, teleseismic body waves and surface waves, are insensitive to vertically extending structures, we cannot confirm whether such a fault exists. However, the existence of such a fault near the subducting KPR, which presumably produces numerous faults in the overriding plate (Dominguez et al., 1998; Sun et al., 2020), seems reasonable. Our results indicate that the fault has a NNW–SSE trend (Figure 7a),

roughly parallel to the ridge axis. In addition, the deeper lithological boundaries on the western side suggest a northeast-dipping thrust fault (we do not consider a southwest-dipping normal fault because of the tectonic compression within the prism). Analog and numerical experiments have demonstrated that back-thrusts mainly occur on the leading flank of the seamount (Dominguez et al., 1998; Sun et al., 2020). At ~2 Ma, before the last change in the convergence direction, the KPR was east of this interpreted fault location (Mahony et al., 2011). The following right-lateral motion might have induced the northeast-dipping back-thrust.

5.3 Fluid reservoir related to ridge subduction

The LVZ identified in this study is discernible in the Vp gradient profile of a previous refraction survey, which extends ~60 km laterally beyond the aperture of the OBS array (Figure 1d). Pursuing similar low-velocity features in other existing seismic refraction profiles will help infer the extension of the LVZ. Figure 9c shows the Vp gradient profiles from Nishizawa et al. (2009) and Nakanishi et al. (2018); negative gradients within the prism are marked by blue horizontal bars. These negative gradients have a lateral extension of >100 km. We conclude that the corresponding LVZ represents a vast fluid reservoir in the accretionary prism. Based on Figure 9a, the reservoir is directly above or slightly to the east of the KPR and seems to correlate with tectonic tremors. However, other profiles (thin black lines in Figure 9a) do not exhibit negative gradient features, although they intersect with those showing such features. This inconsistency may be due to the inherent difficulty of tomography methods in retrieving a thin LVZ under smoothing constraints. These profiles should be quantitatively assessed in the future.

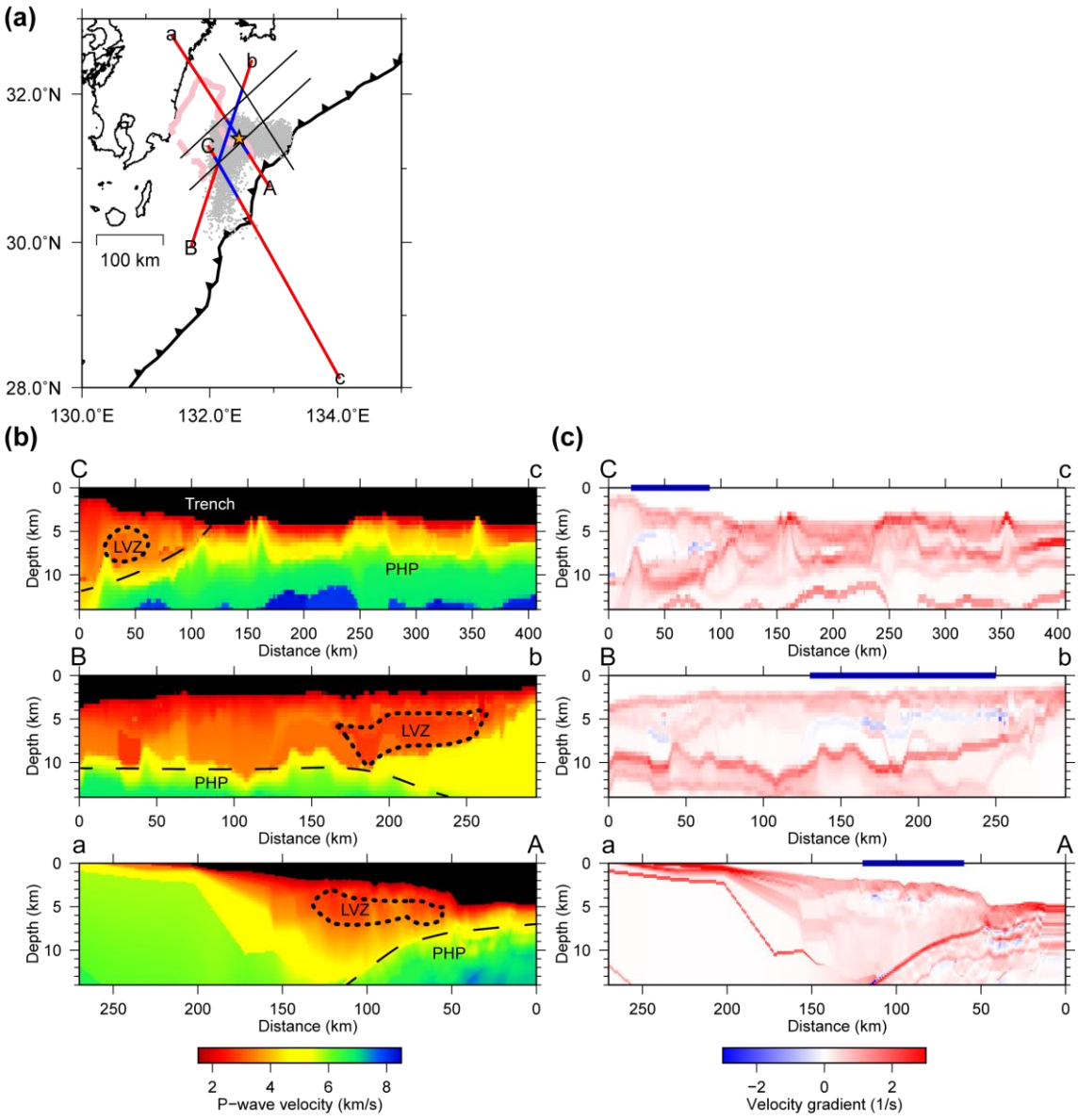

Figure 9. P-wave velocity profiles based on previous refraction seismic surveys. (a) Locations of seismic profiles. The colored lines are the profiles in which negative gradients were identified. The portions with the negative gradients are indicated by blue line segments. The thin black lines are profiles without negative gradients. The gray dots represent the epicenters of tectonic tremors (Yamashita et al., 2015, 2021). The pink line denotes the subducting Kyushu–Palau Ridge (Yamamoto et al., 2013). The orange star denotes the location of an array of ocean-bottom seismometers. (b) P-wave velocity profiles: A–a was obtained from Nakanishi et al. (2018), the same as Figure 1c; B–b and C–c were taken from Nishizawa et al. (2009). The dashed lines represent the plate interface. The dotted lines enclose the low-velocity zone in the accretionary prism. (c) P-wave velocity gradient profiles. The blue horizontal bars highlight the region with a

negative gradient in the prism.

The spatial correlation between the interpreted reservoir (i.e., the region with the negative gradients) and KPR may justify our hypothesis that faults induced by the subduction of the KPR act as fluid pathways. Negative gradients can be observed slightly east of the KPR (along profile B–b), which may reflect the oblique subduction direction starting at ~2 Ma (Itoh et al., 1998; Yamazaki & Okamura, 1989). Furthermore, the intense activity of tectonic tremors below the interpreted reservoir suggests fluid-rich conditions near the subducting plate interfaces (Saffer & Wallace, 2015). Such slow earthquakes reportedly drive nearby fluids into the hanging wall (Tonegawa et al., 2022; Zal et al., 2020), likely contributing to the reservoir in this region.

5.4 Comparison to other tremorgenic regions

In Hyuganada, compacted, well-stratified sediment layers (i.e., U1–3) contribute to the formation of the pronounced reservoir extending over a wide area, which may distinguish Hyuganada from other regions. For example, similar shallow LVZs have not been identified in the outer wedge of the Kumanonada in the central Nankai subduction zone, even above fluid-rich, tremorgenic plate interface (Akuhara et al., 2020; Kitajima & Saffer, 2012; Tsuji et al., 2014). The Hikuragi subduction zone also contains no reservoirs directly above the well-documented tremor source area, where the pore pressure is likely elevated (Arai et al., 2020; Bell et al., 2010). Compared with Hyuganada, these regions are highly deformed and host imbricate thrusts and splay faults. Such thrusts hinder the formation of well-stratified sedimentary layers. Several thrusts are known to penetrate to the ocean bottom, leading to fluid seepage (Park et al., 2002). We conclude that the combination of sufficient water supply from below, permeable structures (i.e., faults), and an impermeable sediment basement above plays a crucial role in reservoir formation.

6. Conclusions

In this study, the Vs structure in the Hyuganada accretionary prism was constrained using a passive seismic array. The Vs structure exhibits a LVZ beneath stratified sedimentary units (U1–3). Based on the reduced Vs and high Vp/Vs ratio, we conclude that the LVZ has a high pore fluid pressure sustained by the impermeable layering above. The significant depth offset of the top of the LVZ, extending over ~4 km of the array aperture, suggests the presence of a blind thrust fault. Based on the seismic refraction profiles, we conclude that the observed LVZ has a lateral extension of >100

km and is a fluid reservoir. Faults generated by the subduction of the KPR act as fluid pathways and contribute to the reservoir.

Although the results of this study demonstrate the potential of passive seismic source analyses with respect to gaining new constraints on fluid processes in the accretionary system, our observations are limited to a narrow region close to the array. In Hyuganda, passive seismic data have been acquired by several OBSs (Tonegawa et al., 2020; Yamashita et al., 2015, 2021). Further analysis of these data will help illuminate the fluid process in this region in more detail.

Acknowledgments

We thank Ryuta Arai for his valuable discussion. This study was supported by JSPS KAKENHI Grant Number 19K14811 and by the Ministry of Education, Culture, Sports, Science and Technology (MEXT) of Japan, under its Earthquake and Volcano Hazards Observation and Research Program.

Data availability

The teleseismic P-waves and ambient noise cross-correlation functions used in this study will be available in an open repository by the time of publication. A computer program for the deconvolution of teleseismic waveforms is available at GitHub repository (https://github.com/akuhara/MC3deconv) or Zenodo repository (https://doi.org/10.5281/zenodo.2548974). A computer program for transdimensional inversion is available at GitHub repository (https://github.com/akuhara/SEIS_FILO) or Zenodo repository (https://doi.org/10.5281/zenodo.6330840). The Vp models of Nishizawa et al. (2009) are available at Database Integrating Seismic Velocity Structure and Plate Geometry Around Japan (https://www.kozo.jishin.go.jp/; see also Yamagishi et al. (2018)). The Vp models of Nakanishi et al. (2018) are available upon request through the JAMSTEC Seismic Survey Database (JAMSTEC, 2004).

References

Agius, M. R., Harmon, N., Rychert, C. A., Tharimena, S., & Kendall, J. M. (2018). Sediment Characterization at the Equatorial Mid-Atlantic Ridge From P-to-S Teleseismic Phase Conversions Recorded on the PI-LAB Experiment. *Geophysical Research Letters*, *45*(22), 12,244-12,252. https://doi.org/10.1029/2018GL080565

Akuhara, T., Bostock, M. G., Plourde, A. P., & Shinohara, M. (2019). Beyond Receiver Functions: Green's Function Estimation by Transdimensional Inversion and Its Application to OBS Data. *Journal of Geophysical Research: Solid Earth*, *124*(2),

1944–1961. https://doi.org/10.1029/2018JB016499

Akuhara, T., Tsuji, T., & Tonegawa, T. (2020). Overpressured Underthrust Sediment in the Nankai Trough Forearc Inferred From Transdimensional Inversion of High-Frequency Teleseismic Waveforms. *Geophysical Research Letters*, *47*(15). https://doi.org/10.1029/2020GL088280

Arai, R., Kodaira, S., Henrys, S., Bangs, N., Obana, K., Fujie, G., et al. (2020). Three-Dimensional P Wave Velocity Structure of the Northern Hikurangi Margin From the NZ3D Experiment: Evidence for Fault-Bound Anisotropy. *Journal of Geophysical Research: Solid Earth*, *125*(12). https://doi.org/10.1029/2020JB020433

Baba, S., Takemura, S., Obara, K., & Noda, A. (2020). Slow Earthquakes Illuminating Interplate Coupling Heterogeneities in Subduction Zones. *Geophysical Research Letters*, *47*(14), 4–5. https://doi.org/10.1029/2020GL088089

Bell, R., Sutherland, R., Barker, D. H. N., Henrys, S., Bannister, S., Wallace, L., & Beavan, J. (2010). Seismic reflection character of the Hikurangi subduction interface, New Zealand, in the region of repeated Gisborne slow slip events. *Geophysical Journal International*, *180*(1), 34–48. https://doi.org/10.1111/j.1365-246X.2009.04401.x

Bensen, G. D., Ritzwoller, M. H., Barmin, M. P., Levshin, A. L., Lin, F., Moschetti, M. P., et al. (2007). Processing seismic ambient noise data to obtain reliable broad-band surface wave dispersion measurements. *Geophysical Journal International*, *169*(3), 1239–1260. https://doi.org/10.1111/j.1365-246X.2007.03374.x

Bodin, T., Sambridge, M., Tkalćić, H., Arroucau, P., Gallagher, K., & Rawlinson, N. (2012). Transdimensional inversion of receiver functions and surface wave dispersion. *Journal of Geophysical Research: Solid Earth*, *117*(2), 1–24. https://doi.org/10.1029/2011JB008560

Brocher, T. M. (2005). Empirical relations between elastic wavespeeds and density in the Earth's crust. *Bulletin of the Seismological Society of America*, *95*(6), 2081–2092. https://doi.org/10.1785/0120050077

Chesley, C., Naif, S., Key, K., & Bassett, D. (2021). Fluid-rich subducting topography generates anomalous forearc porosity. *Nature*, *595*(7866), 255–260. https://doi.org/10.1038/s41586-021-03619-8

Van Dinther, Y., Gerya, T. V., Dalguer, L. A., Mai, P. M., Morra, G., & Giardini, D. (2013). The seismic cycle at subduction thrusts: Insights from seismo-thermo-mechanical models. *Journal of Geophysical Research: Solid Earth*, *118*(12), 6183–6202. https://doi.org/10.1002/2013JB010380

577 Dominguez, S., Lallemand, S. ., Malavieille, J., & von Huene, R. (1998). Upper plate
578 deformation associated with seamount subduction. *Tectonophysics*, *293*(3–4),
579 207–224. https://doi.org/10.1016/S0040-1951(98)00086-9
580 Doran, A. K., & Laske, G. (2019). Seismic Structure of Marine Sediments and Upper
581 Oceanic Crust Surrounding Hawaii. *Journal of Geophysical Research: Solid Earth*,
582 *124*(2), 2038–2056. https://doi.org/10.1029/2018JB016548
583 Dosso, S. E., Dettmer, J., Steininger, G., & Holland, C. W. (2014). Efficient
584 trans-dimensional Bayesian inversion for geoacoustic profile estimation. *Inverse*
585 *Problems*, *30*(11), 114018. https://doi.org/10.1088/0266-5611/30/11/114018
586 Dvorkin, J., Mavko, G., & Nur, A. (1999). Overpressure detection from compressional-
587 and shear-wave data. *Geophysical Research Letters*.
588 https://doi.org/10.1029/1999GL008382
589 Geyer, C. J., & Thompson, E. A. (1995). Annealing Markov Chain Monte Carlo with
590 Appplications to Ancestral Inference. *J. Am. Stat. Assoc.*, *90*(431), 909–920.
591 https://doi.org/10.1080/01621459.1995.10476590
592 Gouédard, P., Cornou, C., & Roux, P. (2008). Phase-velocity dispersion curves and
593 small-scale geophysics using noise correlation slantstack technique. *Geophysical*
594 *Journal International*, *172*(3), 971–981.
595 https://doi.org/10.1111/j.1365-246X.2007.03654.x
596 Green, P. J. (1995). Reversible jump Markov chain monte carlo computation and
597 Bayesian model determination. *Biometrika*, *82*(4), 711–732.
598 https://doi.org/10.1093/biomet/82.4.711
599 Hamilton, E. L. (1979). V_p / V_s and Poisson's ratios in marine sediments and rocks.
600 *The Journal of the Acoustical Society of America*, *66*(4), 1093–1101.
601 https://doi.org/10.1121/1.383344
602 Itoh, Y., Takemura, K., & Kamata, H. (1998). History of basin formation and tectonic
603 evolution at the termination of a large transcurrent fault system: deformation mode
604 of central Kyushu, Japana. *Tectonophysics*, *284*(1–2), 135–150.
605 https://doi.org/10.1016/S0040-1951(97)00167-4
606 JAMSTEC. (2004). JAMSTEC Seismic Survey Database.
607 https://doi.org/10.17596/0002069
608 Kitajima, H., & Saffer, D. M. (2012). Elevated pore pressure and anomalously low stress
609 in regions of low frequency earthquakes along the Nankai Trough subduction
610 megathrust. *Geophysical Research Letters*.
611 https://doi.org/10.1029/2012GL053793
612 Kominz, M. A., Patterson, K., & Odette, D. (2011). Lithology dependence of porosity in

slope and deep marine sediments. *Journal of Sedimentary Research*, *81*(10), 730–742. https://doi.org/10.2110/jsr.2011.60

Mahony, S. H., Wallace, L. M., Miyoshi, M., Villamor, P., Sparks, R. J., & Hasenaka, T. (2011). Volcano-tectonic interactions during rapid plate-boundary evolution in the Kyushu region, SW Japan. *Bulletin of the Geological Society of America*, *123*(11–12), 2201–2223. https://doi.org/10.1130/B30408.1

Mosher, S. G., Eilon, Z., Janiszewski, H., & Audet, P. (2021). Probabilistic inversion of seafloor compliance for oceanic crustal shear velocity structure using mixture density neural networks. *Geophysical Journal International*, *227*(3), 1879–1892. https://doi.org/10.1093/gji/ggab315

Nakanishi, A., Takahashi, N., Yamamoto, Y., Takahashi, T., Ozgur Citak, S., Nakamura, T., et al. (2018). Three-dimensional plate geometry and P-wave velocity models of the subduction zone in SW Japan: Implications for seismogenesis. In T. Byrne, I. Underwood, Michael B., D. Fisher, L. McNeill, D. Saffer, K. Ujiie, & A. Yamaguchi (Eds.), *Geology and Tectonics of Subduction Zones: A Tribute to Gaku Kimura*. Geological Society of America. https://doi.org/10.1130/2018.2534(04)

Nishizawa, A., Kaneda, K., & Oikawa, M. (2009). Seismic structure of the northern end of the Ryukyu Trench subduction zone, southeast of Kyushu, Japan. *Earth, Planets and Space*, *61*(8), e37–e40. https://doi.org/10.1186/bf03352942

Park, J. O., Tsuru, T., Kodaira, S., Cummins, P. R., & Kaneda, Y. (2002). Splay fault branching along the Nankai subduction zone. *Science*, *297*(5584), 1157–1160. https://doi.org/10.1126/science.1074111

Park, J. O., Hori, T., & Kaneda, Y. (2009). Seismotectonic implications of the Kyushu-Palau ridge subducting beneath the westernmost Nankai forearc. *Earth, Planets and Space*, *61*(8), 1013–1018. https://doi.org/10.1186/BF03352951

Prasad, M. (2002). Acoustic measurements in unconsolidated sands at low effective pressure and overpressure detection. *Geophysics*, *67*(2), 405–412. https://doi.org/10.1190/1.1468600

Saffer, D. M., & Wallace, L. M. (2015). The frictional, hydrologic, metamorphic and thermal habitat of shallow slow earthquakes. *Nature Geoscience*, *8*(8), 594–600. https://doi.org/10.1038/ngeo2490

Sahling, H., Masson, D. G., Ranero, C. R., Hühnerbach, V., Weinrebe, W., Klaucke, I., et al. (2008). Fluid seepage at the continental margin offshore Costa Rica and southern Nicaragua. *Geochemistry, Geophysics, Geosystems*, *9*(5). https://doi.org/10.1029/2008GC001978

Sambridge, M. (2014). A Parallel Tempering algorithm for probabilistic sampling and

multimodal optimization. *Geophysical Journal International*, *196*(1), 357–374. https://doi.org/10.1093/gji/ggt342

Stachnik, J. C., Sheehan, A. F., Zietlow, D. W., Yang, Z., Collins, J., & Ferris, A. (2012). Determination of New Zealand Ocean Bottom Seismometer Orientation via Rayleigh-Wave Polarization. *Seismological Research Letters*, *83*(4), 704–713. https://doi.org/10.1785/0220110128

Sun, T., Saffer, D., & Ellis, S. (2020). Mechanical and hydrological effects of seamount subduction on megathrust stress and slip. *Nature Geoscience*, *13*(3), 249–255. https://doi.org/10.1038/s41561-020-0542-0

Tonegawa, T., Araki, E., Kimura, T., Nakamura, T., Nakano, M., & Suzuki, K. (2017). Sporadic low-velocity volumes spatially correlate with shallow very low frequency earthquake clusters. *Nature Communications*, *8*(1), 2048. https://doi.org/10.1038/s41467-017-02276-8

Tonegawa, T., Yamashita, Y., Takahashi, T., Shinohara, M., Ishihara, Y., Kodaira, S., & Kaneda, Y. (2020). Spatial relationship between shallow very low frequency earthquakes and the subducted Kyushu-Palau Ridge in the Hyuga-nada region of the Nankai subduction zone. *Geophysical Journal International*, *222*(3), 1542–1554. https://doi.org/10.1093/gji/ggaa264

Tonegawa, T., Takemura, S., Yabe, S., & Yomogida, K. (2022). Fluid migration before and during slow earthquakes in the shallow Nankai subduction zone. *Journal of Geophysical Research: Solid Earth*. https://doi.org/10.1029/2021JB023583

Tsuji, T., Kamei, R., & Pratt, R. G. (2014). Pore pressure distribution of a mega-splay fault system in the Nankai trough subduction zone: Insight into up-dip extent of the seismogenic zone. *Earth and Planetary Science Letters*, *396*, 165–178. https://doi.org/10.1016/j.epsl.2014.04.011

Wang, K., & Hu, Y. (2006). Accretionary prisms in subduction earthquake cycles : The theory of dynamic Coulomb wedge, *111*(March), 1–16. https://doi.org/10.1029/2005JB004094

Yamagishi, Y., Nakanishi, A., Miura, S., Kodaira, S., & Sakaguchi, H. (2018). Development of a database and visualization system integrating various models of seismic velocity structure and subducting plate geometry around Japan. *Progress in Earth and Planetary Science*, *5*(1). https://doi.org/10.1186/s40645-018-0207-4

Yamamoto, Y., Obana, K., Takahashi, T., Nakanishi, A., Kodaira, S., & Kaneda, Y. (2013). Imaging of the subducted kyushu-palau ridge in the hyuga-nada region, western nankai trough subduction zone. *Tectonophysics*, *589*, 90–102. https://doi.org/10.1016/j.tecto.2012.12.028

Yamashita, Y., Yakiwara, H., Asano, Y., Shimizu, H., Uchida, K., Hirano, S., et al. (2015). Migrating tremor off southern Kyushu as evidence for slow slip of a shallow subduction interface. *Science*, *348*(6235), 676–679. https://doi.org/10.1126/science.aaa4242

Yamashita, Y., Shinohara, M., & Yamada, T. (2021). Shallow tectonic tremor activities in Hyuga-nada, Nankai subduction zone, based on long-term broadband ocean bottom seismic observations. *Earth, Planets and Space*, *73*(1). https://doi.org/10.1186/s40623-021-01533-x

Yamaya, L., Mochizuki, K., Akuhara, T., & Nishida, K. (2021). Sedimentary Structure Derived From Multi-Mode Ambient Noise Tomography With Dense OBS Network at the Japan Trench. *Journal of Geophysical Research: Solid Earth*, *126*(6), 1–20. https://doi.org/10.1029/2021JB021789

Yamazaki, T., & Okamura, Y. (1989). Subducting seamounts and deformation of overriding forearc wedges around Japan. *Tectonophysics*, *160*(1–4), 207–229. https://doi.org/10.1016/0040-1951(89)90392-2

Zal, H. J., Jacobs, K., Savage, M. K., Yarce, J., Mroczek, S., Graham, K., et al. (2020). Temporal and spatial variations in seismic anisotropy and VP/VS ratios in a region of slow slip. *Earth and Planetary Science Letters*, *532*, 115970. https://doi.org/10.1016/j.epsl.2019.115970

Zhang, X., Hansteen, F., Curtis, A., & de Ridder, S. (2020). 1-D, 2-D, and 3-D Monte Carlo Ambient Noise Tomography Using a Dense Passive Seismic Array Installed on the North Sea Seabed. *Journal of Geophysical Research: Solid Earth*, *125*(2), 1–32. https://doi.org/10.1029/2019JB018552